Effects of Adding Forced Near-Inertial Motion to a Wind-Driven Channel Flow

STEPHANNE TAYLOR

Department of Atmospheric and Oceanic Sciences, McGill University, Montreal, Quebec, and Bedford Institute of Oceanography, Fisheries and Oceans Canada, Dartmouth, Nova Scotia, Canada

DAVID STRAUB

Department of Atmospheric and Oceanic Sciences, McGill University, Montreal, Quebec, Canada

(Manuscript received 30 November 2019, in final form 1 August 2020)

ABSTRACT: An eddy-resolving primitive equation ocean model is used to examine energy transfers between frequency bands. Steady wind forcing is used to drive a geostrophic channel to which high-frequency winds are added. This excites near-inertial motion, which exerts a Reynolds stress on the slowly varying flow and acts to transfer kinetic energy between low and high frequencies. These transfers extract balanced energy primarily from the mesoscale. A frequency analysis of the transfers shows the bulk of the energy to be extracted from an intermediate range of frequencies that are large relative to the dominant kinetic energy–containing frequencies and small relative to the spectral gap separating high- and low-frequency bands. This phenomenon is robust and is found in systems spanning two orders of magnitude of kinetic energy. Direct calculation of potential energy transfers proved more difficult but nonetheless shows a similar low-to-high frequency transfer. For the parameter range considered, the ratio of potential-to-kinetic energy transfers is slightly larger than unity, and as such is consistent with balanced energy being extracted from horizontal scales that are somewhat larger than the relevant deformation radius.

KEYWORDS: Ocean dynamics; Numerical analysis/modeling

1. Introduction

Wind-driven ocean circulation is often considered from the perspective of geostrophic dynamics, with both the wind forcing and the ocean response assumed to vary at low frequencies. Realistic wind forcing includes higher-frequency components, and near-inertial (NI) oscillations are often observed to be superimposed on background, nearly geostrophic flow. Recent results suggest that near-inertial motion can interact with the background flow in such a way as to extract energy from the balanced flow in a variety of systems. Because the near-inertial frequency band can readily transfer energy forward in wavenumber space, this interaction can be thought as a route to dissipation for the balanced or nearly geostrophic flow. When the near-inertial frequency band is forced, whether by winds or other processes, it has been suggested that this transfer can compose a significant portion of the dissipation of balanced flow (e.g., Gertz and Straub 2009; Xie and Vanneste 2015, hereinafter XV15; Wagner and Young 2016; Barkan et al. 2017; Grisouard 2018; Rocha et al. 2018).

Observations show that large-scale near-inertial waves are ubiquitous in the ocean and can propagate across oceanic basins (Alford 2003; Alford et al. 2016). Modeling and observational studies suggest that, globally, the power input into the geostrophic flow and near-inertial modes are comparable. For the geostrophic flow, estimates lie between 0.7 and 1.0 TW (Huang et al. 2006; Scott and Xu 2009; Zhai et al. 2012), whereas estimates for near-inertial frequencies give power inputs between 0.3 and 1.4 TW, depending on assumptions made about the structure of the upper ocean (Alford 2001; Jiang et al. 2005; Furuichi et al. 2008; Rimac et al. 2013). As basin and global modeling efforts are increasingly using higher-frequency wind forcing (and finer horizontal and vertical resolution), the near-inertial band is becoming marginally resolved in large-scale models, particularly in the low to mid-latitudes. As such, it is timely to work toward a comprehensive understanding of the effect of near-inertial wind forcing on large-scale circulation patterns, including balance–unbalance interactions at oceanic basin scales.

Near-inertial motion is part of the unbalanced flow and because of a forward cascade in wavenumber space, unbalanced modes dominate at large wavenumber (Rocha et al. 2016; Alford et al. 2016). By contrast, mesoscale flow is dominated by balanced motion, and as such there is a tendency to associate balance with large scales and imbalance with small scales. This, in effect, allows for a separation of both spatial and temporal scales, which has led many studies to make use of the Wentzel–Kramers–Brillouin (WKB) approximation. By separating the flow according to both spatial and temporal scales, Bühler and McIntyre (2005) built a framework showing that a wave packet propagating through a background balanced flow extracts energy from the background, and can ‘‘freeze’’ in place. Aside from the strict separation of scales required by the use of the WKB approximation, their framework is very general and forms a foundation for much of the work concerning internal waves extracting energy from background flows. The WKB approximation also allows for a straightforward decomposition of the flow into a front and waves, and in systems where it can be applied, waves can extract balanced energy from the front (e.g., Thomas 2012). Other mechanisms have also been shown to allow for a transfer of energy from a geostrophically

---

Corresponding author: Stephanne Taylor, stephanne.taylor@dfo-mpo.gc.ca

DOI: 10.1175/JPO-D-19-0299.1

balanced front to near-inertial waves, including critical reflection off the surface (Grisouard and Thomas 2015, 2016) and lateral shear (Whitt and Thomas 2013, 2015).

The requirement that the waves have smaller spatial scales than the background is not always physically justified. Although near-inertial frequencies are dominant only at small scales, a large fraction of near-inertial energy in fact resides at larger scales. It is plausible that large-scale near-inertial motion interacts more readily with mesoscale currents and eddies, and this motivates relaxing the assumptions inherent to the WKB approximation. Note that a separation of frequency scales is still necessary for balanced and unbalanced energy to be clearly defined.

With this in mind, Young and Ben Jelloul (1997, hereinafter YBJ97) constructed a framework describing the evolution of near-inertial oscillations in an (uncoupled) quasigeostrophic (QG) background flow. Their equations do not formally require a separation of spatial scales between the two regimes, but instead rely on a careful expansion in terms of the two characteristic time scales. XV15 use a generalized Lagrangian mean formulation to expand YBJ97 to describe a coupled system of QG flow with near-inertial waves, explicitly allowing the near-inertial modes to feedback on to the balanced flow. The XV15 formulation is formally required to have a small Rossby number, allowing for averages over the near-inertial time period; this phase-averaging is key for reducing their equations to a tractable form. In this framework total energy and near-inertial kinetic energy (KE) are separately conserved. As such, an increase in near-inertial potential energy (PE) implies a loss of mechanical balanced energy. They find this transfer to be robust when near-inertial motion is externally forced. However, other work has suggested that this transfer may be relatively weak in some contexts (Asselin and Young 2020).

Wagner and Young (2016) also extend the YBJ97 framework to include the second harmonic of near-inertial flow (i.e., flow with frequencies $\sim 2f_0$). This harmonic plays a critical role in generating near-inertial motion with small vertical scales in a constrained system: when the $2f_0$ modes gain energy, there is a transfer of energy via a parametric subharmonic instability to the near-inertial modes. Small vertical scales are a commonly observed feature of near-inertial motion, and two-component models like YBJ97 (which neglect the $2f_0$ band) do not efficiently reproduce this structure. The Wagner and Young (2016) framework is used by Rocha et al. (2018) to consider a barotropic turbulent flow with a plane wave near-inertial flow. Wave potential energy is generated in their system by refraction as well as geostrophic straining, both of which result in a loss of balanced energy. They find that the bulk of the loss of balanced energy is due to geostrophic straining, but wave refraction is still key: refraction generates the gradients in the wave field that allow the straining to occur efficiently. They mostly consider a turbulent regime; however, they briefly consider a nonturbulent balanced flow. Without the continual stirring of lateral gradients inherent in turbulent flows, they find that the conversion of energy may flow in either direction. In a modeling study of the unstratified ocean double gyre problem, Gertz and Straub (2009) found something similar: near-inertial forcing in energetic regions of the gyres led to a dissipation of balanced energy, whereas near-inertial motion in more quiescent regions led to a forcing.

The first-order-accurate YBJ97 framework is extended to second-order accurate by Asselin and Young (2019), who also couple the QG and near-inertial flows. In their "YBJ+" framework, the Rossby and Burger numbers are now independently constrained, which allows them to cover a larger range of physically relevant parameter space than with YBJ97. The additional terms in the equation do not add much computational complexity over YBJ97, but more accurately reproduce a modeled Boussinesq flow. They then use this framework to consider how poststorm near-inertial waves propagate in in a background flow with a realistic stratification profile in Asselin and Young (2020). Consistent with previous work, they find that anticyclones act as "drainpipes," funneling wave kinetic energy from the source at the surface into the ocean interior. Most of the wave kinetic energy remains at the base of the mesoscale baroclinic eddies that facilitated its downward propagation (see their Figs. 6 and 9), and a significant portion of the wave KE is eventually found below 1 km depth. It is unclear what proportion of this wave KE, if any, is due to an extraction of energy from balanced flow rather than (attenuated) propagation down the water column.

Analytic studies can provide elegant frameworks for understanding balance–unbalance interactions, but they can also require diagnostics that may be difficult to implement in Eulerian numerical models. Modeling studies are useful in that they allow for consideration of a wide range of regimes, including some in which explicit assumptions of the analytic methods are not formally valid. Taylor and Straub (2016, hereinafter TS16) used a primitive equation model forced with a combination of a steady and near-inertial wind to again show that there is a transfer of energy from balanced to unbalanced motion. Both the steady and near-inertial winds are associated primarily with large spatial scales, and a transfer of energy (which they termed the "advective sink") out of the balanced flow occurs mainly at these length scales. They found the advective sink to be robust across a range of systems with varying levels of kinetic energy.

Barkan et al. (2017) also take a modeling approach, but use a smaller domain, a large Rossby number, and submesocale resolution so that a continuum of small scale interactions is resolved. Their configuration yields a relatively weak near-inertial peak, and the balanced and near-inertial components are separated using a Gaussian filter. They find that the addition of near-inertial forcing leads to an increase in dissipation that is larger than the additional energy source, indicating that the near-inertial motion extracts energy from the background flow. By changing the width of the filter that separates near-inertial and balanced flow, they find that about half of this excess dissipation is extracted from low frequencies, with the remainder coming from frequency bands adjacent to the near-inertial range.

There remains ambiguity as to whether all of these results are variations on the same mechanism, or whether there is a variety of mechanisms that are relevant in the various systems considered. Both TS16 and Barkan et al. (2017) focus on the KE budget, and include both the sink terms found in the balanced KE equation and the source terms of equal size in the unbalanced KE equation. By contrast, the XV15 framework explicitly filters out transfers to or from unbalanced KE, making it unclear whether their mechanism may be distinct from other modeling work. Their framework requires conservation of unbalanced KE, but does not exclude the possiblity that transfers from balanced-to-unbalanced KE may be compensated by transfers from KE to PE within the unbalanced pool. Modeling work by M. Claret (2015, personal communication) suggests that there may be a minimal net increase of unbalanced KE when a near-inertial oscillation interacts with in a two-dimensional front. Similarly, Rocha et al. (2018) note that the generation of unbalanced potential energy via Reynolds shear production (RSP) can be consistent with both a barotropic balanced flow and conserved wave KE, provided that the unbalanced energy is extracted as kinetic energy and then entirely converted to potential energy. Their RSP is equivalent to the horizontal component of the advective sink of TS16 and this work; note that TS16 found the vertical component of their advective sink to be dominant.

Different studies have focused on different portions of the energy budget, but most are primarily concerned with the kinetic energy. Grisouard (2018), by contrast, focuses on potential energy. He considers a constant stratification and finds robust potential energy transfers out of a submesoscale front, consistent with the body of work largely focused on kinetic or total energy. This robust transfer of potential energy via geostrophic buoyancy production can be larger than the balanced-to-unbalanced transfer of kinetic energy. XV15 and similar models separate unbalanced (but not balanced) energy into kinetic and potential pools, and also assume prescribed stratification profiles.

Here, we wish to emphasize two points. First, near-inertial motion can impact the base-state stratification. These changes can be large, and arguably represent a more profound impact of near-inertial forcing on the system than that relating to extraction of balanced energy. These changes in stratification also make direct comparison with more idealized models more difficult, since these models typically do not allow for stratification that evolves in time. Second, if balanced flow remains reasonably close to quasigeostrophy, then extraction of balanced kinetic and potential energy occurs in a ratio determined by the horizontal and vertical scales of the energy being extracted. That is, for a given vertical mode, the ratio of kinetic-to-potential energy is given by the squared ratio of the deformation radius for the mode in question to the horizontal length scale. It then seems natural to suggest that extraction of balanced kinetic and potential energy occur in roughly this same ratio. By this argument, extraction of kinetic energy from length scales comparable to or larger than the deformation radius of the first baroclinic mode should imply an even larger extraction of balanced potential energy.

There have been several terms coined to describe these various balance–unbalance interactions that are robustly seen in a variety of systems, and it is worth clarifying the relation between them. Stimulated loss of balance (SLOB) was introduced by XV15 and emphasizes the external forcing of unbalanced motion, making no assumptions about the scale separation between balanced and unbalanced flow. We take this to be a general term, with the advective sink of TS16 being a particular example. The advective sink appears to be equivalent to Barkan et al.'s (2017) "direct extraction." Barkan et al.'s (2017) use of "stimulated imbalance" is more specific and refers to only the effect of a forward cascade in frequency space induced by the presence of near-inertial forcing. Finally, Rocha et al. (2018) point to a quantum mechanics analogy and use "stimulated generation" to refer to this process in models similar to theirs and that of XV15.

In this paper, we seek to refine and expand the work presented in TS16, and as such we largely retain their model configuration. We use a primitive equation model to simulate a recirculating channel at high latitudes. The model is forced with a combination of steady and near-inertial winds that drive geostrophic flow and near-inertial flows, respectively. We are particularly interested in the Reynolds stresses exerted by the near-inertial modes on the geostrophic flow and analogous nonlinear transfer terms in the potential energy equation. We refine our previous eddy-permitting simulations by increasing both horizontal and vertical resolution. Consistent with TS16, we find that the high-frequency components of the flow exert Reynolds stresses that serve both to extract and vertically redistribute kinetic energy of the low-frequency flow.

Section 2 describes our system in detail. Section 3 details the kinetic energy budget, and the kinetic advective sink is discussed in section 4. Section 5 discusses potential energy and the potential advective sink. We discuss our results in section 6.

2. Model and experimental design

We consider a wind-driven channel flow in a spherical coordinate primitive equation model [Parallel Ocean Program (POP)]. The 4000-m-deep channel sits at high latitudes, spanning from 43° to 67°S and covering 60° of longitude. Bottom topography is a meridionally aligned Gaussian ridge, with a height of 1.785 km and a decay scale of 8.25°. The critical difference between the setup of this work and TS16 is resolution: here, we increase the horizontal resolution from 1/10° to ~1/20° and use 30 vertical levels ranging from 10 to 300 m thick. The meridional resolution is 5.05 km, and the zonal resolution varies from 6.2 km at the equatorward edge of the domain to 3.3 km at the poleward side; this setup isotropizes the grid as much as possible, given the use of spherical coordinates at high latitudes. The radius of deformation ranges between 20 and 22 km for all of our base-state simulations, consistent with typical values found in the Southern Ocean (Tulloch et al. 2009). As such, our simulations can be considered eddy resolving.

We use a single component linear equation of state. Temperature is initialized with a profile calculated using the Levitus data: the Levitus data are used to generate a density profile, and this density, together with a constant salinity set to 35 psu, is used to calculate the initial temperature profile. We apply biharmonic viscosity in the horizontal to remove small-scale momentum and tracer variance, vertical viscosity calculated using a K-profile parameterization (KPP) scheme (Large et al. 1994), and quadratic bottom drag. Model parameters and settings are listed in Table 1.

TABLE 1. Various model parameters and settings.

Model parameter	Parameter value
Zonal grid spacing	3.3–6.2 km
Meridional grid spacing	5.05 km
Vertical grid spacing	10–300 m
Time steps per day	500
Mixing interval	17
Coriolis parameter	$f_0 = 1.18 \times 10^{-4}\,\mathrm{s}^{-1}$ $f_{\min} = 0.99 \times 10^{-4}\,\mathrm{s}^{-1}$, $f_{\max} = 1.34 \times 10^{-4}\,\mathrm{s}^{-1}$
Quadratic bottom drag coef	2.5×10^{-3}
Horizontal biharmonic viscosity momentum coef	$-8.0 \times 10^{12}\,\mathrm{cm}^4\,\mathrm{s}^{-1}$
Horizontal biharmonic viscosity tracer coef	$-4.0 \times 10^{12}\,\mathrm{cm}^4\,\mathrm{s}^{-1}$
KPP upper background diffusivity	$0.250\,\mathrm{cm}^2\,\mathrm{s}^{-1}$
KPP lower background diffusivity	$0.025\,\mathrm{cm}^2\,\mathrm{s}^{-1}$
KPP transition depth	1700 m
KPP variation inverse length scale	$0.0050\,\mathrm{m}^{-1}$
Advection scheme	Third-order upwind
Gaussian ridge parameters	$x_o = 30°$; height = 1.785 km; $\sigma = 8.25°$

We use the same wind forcing as in TS16, that is, a zonal wind with steady and near-inertial components. The steady wind has a sinusoidal meridional profile and is strongest in the middle of the channel:

$$\tau_{\mathrm{steady}} \equiv \tau_0[1 + \cos(2\pi y/L)], \quad \text{with} \quad y/L = \frac{\theta - \theta_0}{\Delta\theta}, \qquad (1)$$

where θ_0 is the latitude of the middle of the channel and $\Delta\theta$ is the difference in latitude between the edges of the fluid. We use four values of τ_0: 0.30, 0.15, 0.03, and $0.015\,\mathrm{N\,m}^{-2}$. The first three values correspond to the strong, medium, and weak base-state wind stresses from TS16, so we retain the naming conventions of TS16 and refer to the four wind stresses as strong, medium, weak, and very weak, respectively. The medium value of $\tau_0 = 0.15\,\mathrm{N\,m}^{-2}$ corresponds roughly to the average wind stress over the Southern Ocean in winter (Li et al. 2013; Huang et al. 2006; Josey et al. 2002). We emphasize that our simulations are not meant to directly model the Southern Ocean, but rather that we use physically realistic parameters to generate physically reasonable and oceanographically relevant flows. Our strong base state is very strong, but we wanted to explore as large a parameter space as possible.

The near-inertial wind is as in TS16. It forces in the near-inertial band only and has no steady or low-frequency component. It has no horizontal structure, and is given by

$$\tau_{\mathrm{NI}}(t) \equiv \xi\tau_0 \sum_{n=1}^{N} \mu_n \sin(\omega_n t + \Phi_n), \quad \text{where}$$

$$\mu_n = \frac{1}{\sqrt{N}} e^{\nu_n^2} \quad \text{and}$$

$$\nu_n = \frac{\omega_n - f_0}{\sqrt{2}\sigma}. \qquad (2)$$

Here, f_0 is the Coriolis frequency at the middle of the channel, ω_n ranges from $f_0/2$ to $2f_0$ and is linearly sampled with N = 10 000, $\sigma = f_0/6$ is the width of the modulating Gaussian envelope μ_n, and Φ_n is a random phase. The Gaussian envelope ensures that the frequencies closest to the mid-channel inertial frequency are forced most strongly, and using a high rate of sampling ensures that the winds can be considered quasi-stochastic. We use three nonzero values of ξ to specify the strength of the near-inertial forcing: $\xi = \{0, 0.2, 0.35, 0.5\}$. The $\xi = 0$ runs are referred to as the control runs, and ξ is unitless.

The model is spun up with only the steady wind forcing for 20, 40, 85, and 125 years for $\tau_0 = \{0.30, 0.15, 0.03, 0.015\}\,\mathrm{N\,m}^{-2}$, respectively; based on the evolution of kinetic energy and dissipation diagnostics this was sufficient to reach a quasi equilibrium, in which the change in total kinetic energy oscillates around a relatively static value that changes minimally from one year to the next. The weaker values of τ_0 required longer spinups since the flow is less energetic and therefore takes longer to equilibrate. After spinup, we force the model for an additional 2 years with the combined steady and near-inertial forcing to allow the flow to adjust to the near-inertial winds. Following this adjustment, we continue to force the model with both steady and near-inertial winds for a further 27 months; only these data are used for analysis.

Figure 1 shows typical snapshots of the flow in the middle of the 27-month data collection window for the medium base state ($\tau_0 = 0.15\,\mathrm{N\,m}^{-2}$). Figure 1a shows the full flow for the control run, with partial topographic contours overlaid in white at intervals of 250 m. Figure 1b shows the high-frequency flow for the medium base state with $\xi = 0.35$; note that the high-frequency kinetic energy is relatively evenly distributed throughout the domain. For our data analysis, we output snapshots of various kinetic and thermodynamic quantities ten times a day, compile these snapshots into time series, and then use Fourier methods to decompose quantity X into low-frequency ($X^{<}$) and high-frequency ($X^{>}$) components. The time series we collect are twice as long as those in TS16, and this combined with the higher resolution means that the statistics converge more

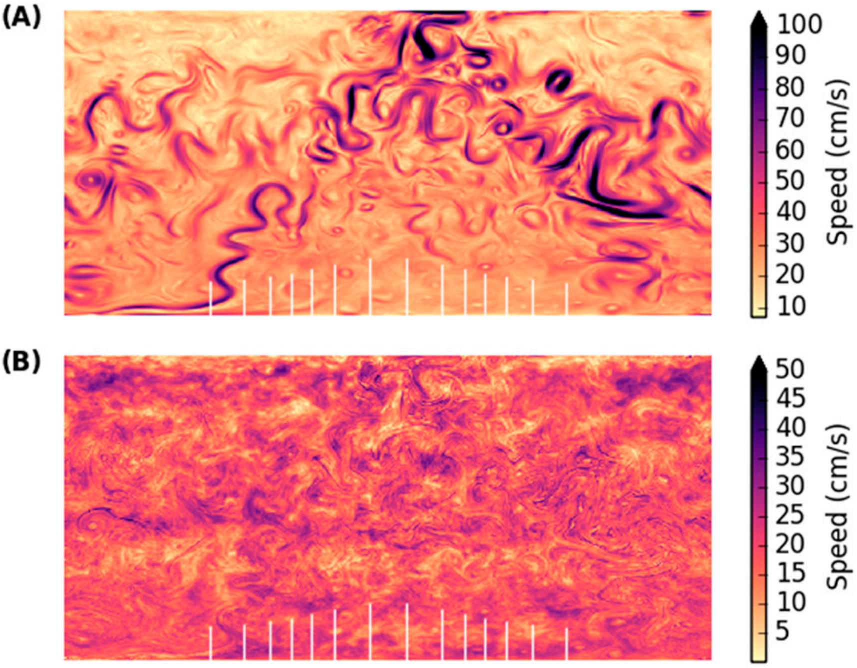

FIG. 1. Typical snapshots of surface speed ($\mathrm{cm\,s^{-1}}$): (a) control run and (b) the high-frequency flow for the medium base state with $\xi = 0.35$. White ticks at the bottom of the panels indicate meridional topography contours at 250-m intervals, with the highest contour corresponding to a depth of 2250 m. The channel spans 60° longitude and 24° latitude.

quickly; as such, we use ensembles of three simulations for each combination of τ_0 and ξ.

Much of this paper is focused on further exploring the advective sink of TS16, which allows for near-inertial flow to add or remove low-frequency kinetic energy. We define $\mathbf{v}$ to be the three-dimensional velocity and $\mathbf{u}$ to be its horizontal projection: $\mathbf{v} = \mathbf{u} + w\hat{\mathbf{z}}$. The kinetic energy equation is found by taking the scalar product of $\mathbf{v}$ with the momentum equation. For the hydrostatic system we consider, terms involving the vertical component of the momentum equation cancel identically, so that the kinetic energy equation is given by

$$\begin{aligned}\frac{d}{dt}\left(\frac{1}{2}\mathbf{u}\cdot\mathbf{u}\right) &= -\mathbf{v}\cdot(\mathbf{v}\cdot\nabla)\mathbf{u} - \mathbf{v}\cdot\nabla p + wb\\ &= -\mathbf{u}\cdot(\mathbf{v}\cdot\nabla)\mathbf{u} - \mathbf{u}\cdot\nabla p,\end{aligned} \tag{3}$$

where viscous terms have been neglected.

The advective sink comes from an expansion of the advective terms into low- and high-frequency parts:

$$\begin{aligned}\mathbf{v}\cdot\nabla\mathbf{u} &= [(\mathbf{v}^{<} + \mathbf{v}^{>})\cdot\nabla](\mathbf{u}^{<} + \mathbf{u}^{>})\\ &= (\mathbf{v}^{<}\cdot\nabla)\mathbf{u}^{<} + (\mathbf{v}^{>}\cdot\nabla)\mathbf{u}^{>} + \text{cross terms}.\end{aligned} \tag{4}$$

The $(\mathbf{v}^{>}\cdot\nabla)\mathbf{u}^{>}$ term involves high-frequency velocity components only, but the dot product contains low frequencies and thus can feed back onto low-frequency kinetic energy. Referring to the second line of Eq. (3), this feedback is given by

$$\chi \equiv -\mathbf{u}^{<}\cdot[(\mathbf{v}^{>}\cdot\nabla)\mathbf{u}^{>}]^{<}, \tag{5}$$

which we call the advective sink. To be consistent with the model numerics, all advective components are calculated in flux form. For example, we calculate χ as

$$\begin{aligned}\chi &= -\mathbf{u}^{<}\cdot[\nabla\cdot(\mathbf{v}^{>}\mathbf{u}^{>})]^{<}\\ &= -u^{<}[\nabla\cdot(\mathbf{v}^{>}u^{>})]^{<} - v^{<}[\nabla\cdot(\mathbf{v}^{>}v^{>})]^{<},\end{aligned} \tag{6}$$

where u and v are the eastward and northward components of $\mathbf{u}$.

An analog to χ appears in the high-frequency kinetic energy equation. This is given by

$$\chi_{\mathrm{HF}} \equiv -\mathbf{u}^{>}\cdot(\mathbf{v}^{>}\cdot\nabla)\mathbf{u}^{<}. \tag{7}$$

The advective sink and its analog, χ_{HF}, integrate to equal and opposite values. Large negative values of χ correspond to loss of low-frequency energy and large positive values of χ_{HF} correspond to energy gain in high-frequency modes. Numerically, χ_{HF} is calculated in a manner similar to that for χ.

The horizontal wavenumber structure of the advective sink (and similar quantities) can be analyzed by calculating the transfer spectra. For example, the transfer spectrum of χ is given by

$$\begin{aligned}&T(\kappa) = \mathbb{R}(A\cdot B^*), \quad \text{where}\\ &A = \mathcal{F}[\mathbf{u}^{<}] \quad \text{and}\\ &B = \mathcal{F}^*[\nabla\cdot(\mathbf{v}^{>}\mathbf{u}^{>})^{<}];\end{aligned} \tag{8}$$

here, κ is the horizontal wavenumber, $\mathbb{R}$ indicates the real component, $\mathcal{F}[]$ indicates a Fourier transform, and the asterisk indicates complex conjugate. The zonal grid spacing at the middle of the channel is approximately equal to the meridional grid spacing, which is constant throughout the domain. However, because we work in spherical coordinates, the zonal grid spacing is larger at the equatorward edge of the channel than at the poleward edge. To account for the latitude dependence of the zonal grid spacing, we again use the adjusted 2D FFT scheme from TS16 (see appendix B in TS16 for details). Briefly, this scheme splits the 2D FFT calculation into three parts: a 1D zonal FFT at each latitude, a reorganization of the data so that the zonal bins correspond to consistent physical wavelengths at all latitudes, and then a 1D meridional FFT. As our grid is as isotropic as possible, this adjustment results in only a small correction to our spectra.

We will also be interested in kinetic energy added or removed via buoyancy production (wb) or, equivalently, by the $\mathbf{u}\cdot\nabla p$ term in the second line of Eq. (3). Transfer spectra for these two terms are the same. Equivalently, transfer spectra for the three-dimensional pressure work term in the first line of Eq. (3) vanish identically as a result of the incompressibility constraint. To be consistent with model numerics, we calculate buoyancy production terms in the kinetic energy equation using $\mathbf{u}\cdot\nabla p$ rather than with wb, but will nonetheless refer to this term as a buoyancy transfer or buoyancy production.

3. Kinetic energy

To characterize the flow regime, we first calculate a balanced (low frequency) kinetic energy budget. The steady wind adds KE to both the geostrophic and Ekman flows. Energy input to the Ekman flow is dissipated by the vertical eddy viscosity, and these terms comprise a larger portion of the total budget in more energetic base states. All domain-integrated terms in the KE budget are normalized by the *total* wind power input into the control system of the same base state, allowing us to more easily compare budgets between systems spanning two orders of magnitude of energy. Figure 2a shows the wind power input into the geostrophic flow, and consistent with a stronger Ekman flow, the more energetic base states have lower proportionate values. This normalization by total wind power input from the appropriate control run is used throughout the rest of this work, whenever domain-integrated quantities are discussed.

For some terms (viz., wind input, bottom drag, and horizontal and vertical viscous dissipation), it is convenient to use the geostrophic velocity as a proxy for $\mathbf{u}^<$. As in TS16, the balanced KE budget is dominated by four terms when $\xi > 0$: (i) the steady wind input, (ii) bottom drag, (iii) the advective sink, and (iv) the low-frequency horizontal pressure gradient. When no near-inertial forcing is present, the advective sink is negligible. These four terms are plotted as functions of ξ for all base states in the first three panels of Fig. 2: Fig. 2a shows the wind input and bottom drag, Fig. 2b shows the advective sink, and Fig. 2c shows the buoyancy transfer (positive values correspond to a production of KE, i.e., to a potential-to-kinetic energy conversion within the balanced pool).

The wind input is largely balanced by bottom drag, with the residual being nearly an order of magnitude smaller than either term. This residual is well approximated by the sum of the advective sink and buoyancy production terms, which are comparable in magnitude and opposite in sign. Figure 2b shows that χ has a clear dependence on base state, with more energetic flows producing more efficient advective sinks. However, even the very weak base state exhibits a significant advective sink, corresponding to about 5% of the balanced KE budget. Full details of the kinetic energy budgets for the medium base-state ensembles are presented in the appendix.

For all base states, adding near-inertial forcing increases the total balanced kinetic energy by 5%–10%, with more NI forcing leading to a slightly larger increase in $\mathrm{KE}^<$. This is shown in Fig. 2d, which plots $\mathrm{KE}^<$ as a function of $\mathrm{KE}^>$ for all four base states; the value of $\mathrm{KE}^<$ for each of the control runs is indicated with a dashed line of the appropriate color. Note the logarithmic x axis: the weaker base states show a weaker response to the near-inertial forcing than do the stronger base states. The four base states span two orders of magnitude in both $\mathrm{KE}^<$ and $\mathrm{KE}^>$, suggesting that our results are relevant for a wide range of oceanographic contexts.

In all of our simulations, kinetic energy increases with ξ. This is at odds with most of the regimes considered in our previous, coarser resolution simulations (TS16). An exception was the weak base in that study. For that case, both $\mathrm{KE}^<$ and the low-frequency buoyancy production term (equivalent to $-\mathbf{u}^<\cdot\nabla P^<$) increased with ξ. In TS16, the weak base state had a relatively large deformation radius and so was closer to an eddy-resolving (than an eddy-permitting) regime than were the other base states they considered. Our resolution here is higher in both the horizontal and vertical. To test which is responsible for the increased buoyancy production source of $\mathrm{KE}^<$, we conducted a small number of simulations using the same eddy-resolving horizontal resolution, but with the coarser vertical resolution used in TS16. These experiments suggested that the changes in the pressure gradient term relative to TS16 are primarily related to horizontal resolution, i.e., now being in an eddy-resolving regime instead of the eddy-permitting regime of TS16.

4. The advective sink

The advective sink extracts and vertically redistributes balanced kinetic energy. Its magnitude depends on τ_0, but broadly speaking its horizontal and vertical structure do not. Vertical profiles of the horizontally averaged χ are presented in Figs. 3a and 3b, and show that balanced kinetic energy is extracted from the near-surface ocean. A substantial portion of this kinetic energy is deposited slightly deeper down (~1–200 m). The net effect is thus to both extract and redistribute balanced (kinetic) energy within the water column.

This reversal just below the mixed layer was seen in TS16 (see their Fig. 4) but is not widely observed or reported elsewhere. It is unclear, for example, whether this vertical redistribution is absent in phase-averaged models like Asselin and Young (2020) or whether it may be present but is simply not reported in these studies. They use a realistic N^2 profile and high resolution, and they find near-inertial energy exits the mixed layer in anticyclonic drainpipes. It would be interesting to investigate whether the distribution of near-inertial energy that results is consistent with a change in sign of our advective

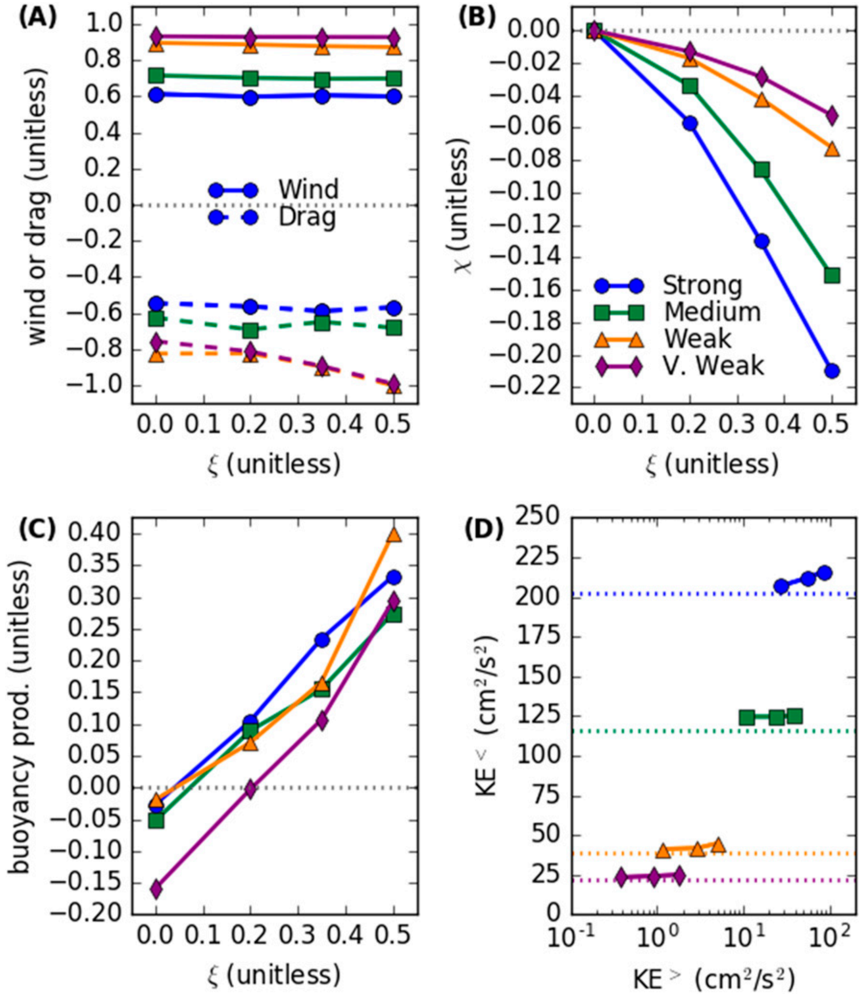

FIG. 2. The kinetic energy budget for the balanced flow (viscosity is omitted). Wind input and bottom drag are calculated using geostrophic flow, and the advective sink and buoyancy production are calculated with low-passed flow. (a) Steady wind input (solid lines) and dissipation by bottom drag (dashed lines). Their sum is primarily balanced by (b) the advective sink and (c) buoyancy production. (d) The $KE^<$ as a function of $KE^>$, with dashed lines indicating the value of $KE^<$ in the relevant control run. Note that the range of base states spans nearly two orders of magnitude of balanced kinetic energy. The color scheme is consistent across all panels.

sink or whether the small loss of balanced energy they observe might be the sum of somewhat larger but opposite-signed terms in and below the surface layer.

Horizontal transfer spectra at the surface are shown in Figs. 3c and 3d. For all base states, χ removes low-frequency energy from the mesoscale: the upper-ocean transfer spectra consistently peak at around $\kappa = 30$ which corresponds to a wavelength of about 130 km. Larger peaks are seen for stronger base states (Fig. 3c) and for stronger near-inertial forcing (Fig. 3d). Consistent with Kafiabad and Bartello (2018), the scales at which energy is removed from the balanced flow do not depend on base state or the amount of near-inertial forcing (see their Fig. 5a). Since their system relies on the spontaneous generation of unbalanced (near-inertial) motion, this suggests that the properties of the observed transfer are not necessarily dependent on the specific mechanism by which near-inertial flow is generated. Figures 3e and 3f show energy spectra for $KE^<$. For all base states considered, the advective sink is most efficient at wavenumbers that are larger by about a factor of 3 than the characteristic wavenumber of $KE^<$.

In the upper ocean, the spectra have a consistent shape, with the amplitude of the curve decreasing with depth. Below the mixed layer, the sign reverses and the spectral peak shifts to lower wavenumbers. In the deep ocean, the spectra are noisy, flat, and values at most κ are positive. Transfer spectra for χ_{HF} show that energy transferred out of the $KE^<$ pool is deposited into the $KE^>$ pool by at slightly higher wavenumbers (not shown). This basic scenario holds throughout the water column

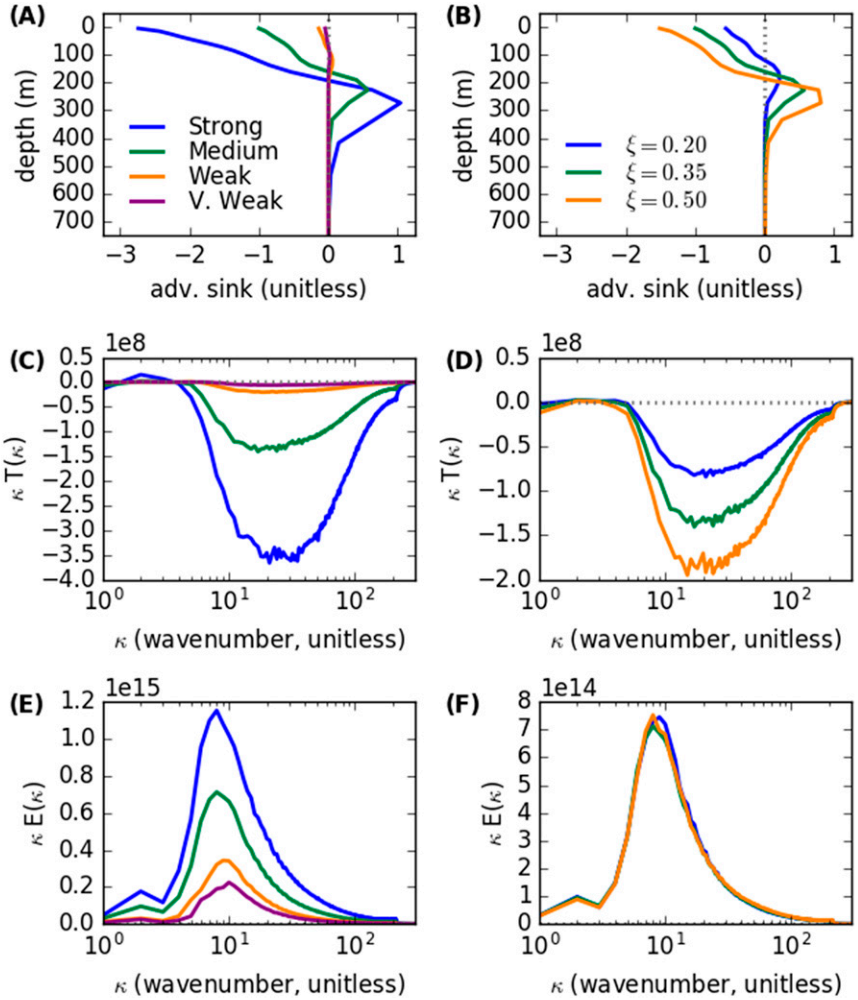

FIG. 3. The spatial structure of the advective sink. Shown are (left) data for $\xi = 0.35$ and a variety of base states and (right) data for the medium base state for three values of ξ. (a),(b) Vertical profiles of the advective sink; values in the lower ocean are small. (c),(d) Horizontal transfer spectra at the surface. (e),(f) Energy spectra for the low-frequency KE; note that the energy-containing length scales are larger than the length scales associated with the advective sink. All spectra are plotted as κE vs κ on semilogarithmic axes, which gives a visual estimate of which wavenumbers contribute most to the energy spectrum; the area under the curve is then an approximation of E.

for all base states, even when the transfer is relatively small. Also evident from χ_{HF} is a transfer of unbalanced energy toward small scales in a manner consistent with recent results from Barkan et al. (2017) and Kafiabad and Bartello (2018, see their Fig. 2b).

The advective sink is robust and significant, but it is unclear from our calculation whether the mechanism generating the sink is primarily, in the language of Barkan et al. (2017), direct extraction or stimulated imbalance. Does the bulk of the extraction occur at frequencies adjacent to the near-inertial range, as with stimulated imbalance, or does it jump across a band of frequencies, as with direct extraction? To estimate the relative contributions of the two mechanisms, we add intermediate frequency bands. The high-frequency band remains the same as before, containing all frequencies higher than $\omega = 1$. The low-frequency band, however, is redefined to include only frequencies lower than $\omega_i = \{1/2, 1/4, 1/8, 1/16, 1/32, 1/64\}$. Using this more restrictive definition, we calculate χ_i. Negative values of χ_i then correspond to transfers from frequencies below the threshold value to frequencies greater that $\omega = 1$, i.e., energy jumps over the intermediate frequency band. If direct extraction is the primary mechanism, omitting a small intermediate band will not significantly reduce the advective sink. If stimulated imbalance is the primary mechanism, then a relatively small gap between the low- and high-frequency bands should result in significant reductions of the advective sink.

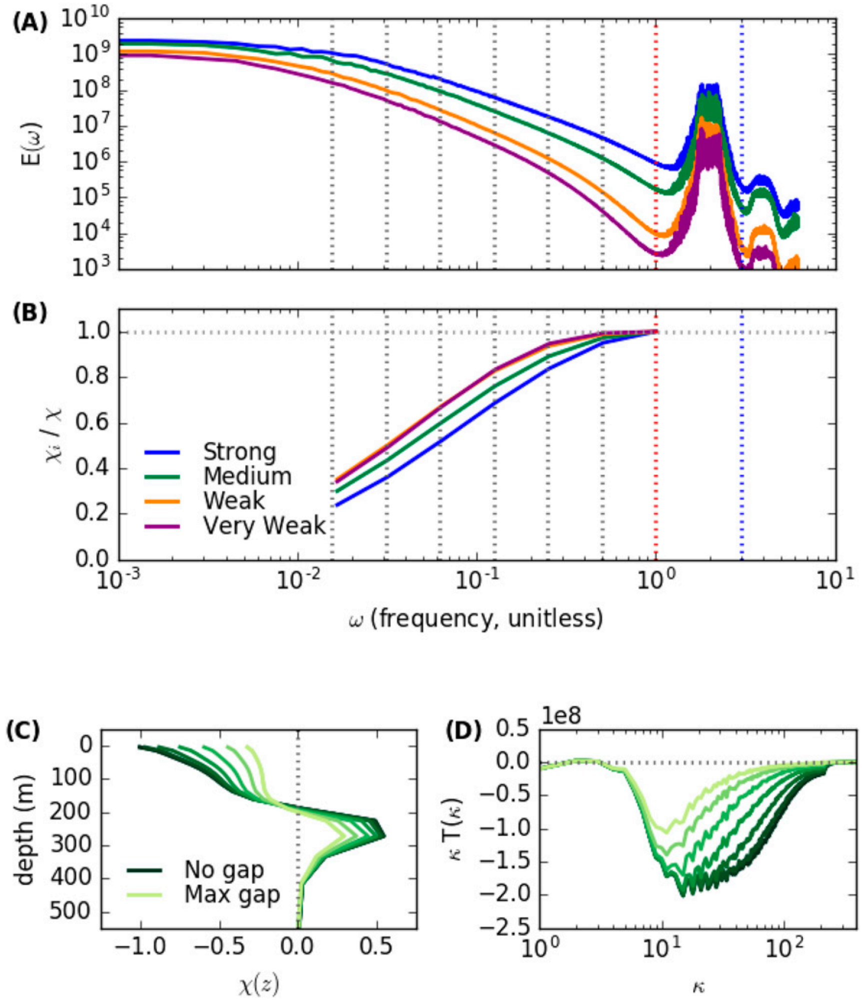

FIG. 4. The advective sink with variable low-frequency bands. (a) A typical frequency spectrum for the kinetic energy, with an orange vertical line at $\omega_0 = 1$ and gray vertical lines at the various values of ω_i. The blue vertical line at $\omega = 3/2$ is the cutoff used to estimate the impact of ignoring the first harmonic of the near-inertial peak. (b) The ratio of χ_i to χ for $\tau_0 = 0.15$ and $\xi = 0.5$. Also shown are (c) the vertical profiles and (d) surface transfer spectra of the range of χ_i for $\tau_0 = 0.15$ and $\xi = 0.5$, with darker green lines corresponding to smaller omitted intermediate bands.

Figure 4a shows frequency power spectra for each base state, with vertical lines added to indicate each of the cutoff frequencies we used. Recall frequencies are normalized such that $\omega = 1$ corresponds a frequency $f = 1/2\ \text{days}^{-1}$, and the inertial peak is centered at $\omega \sim 2$. The frequency spectra shown are for surface kinetic energy, and spectra calculated for other depths in the upper ocean are qualitatively similar. Values of the χ_i, integrated over all vertical levels and calculated with each of these cutoffs, are plotted in 4(b). These are normalized by χ, i.e., the advective sink calculated without a missing frequency band.

The value of χ_i drops off slowly between $\omega_i = 1$ and $\omega_i = 1/4$, suggesting that our advective sink is predominantly direct extraction. The trend in χ_i then goes roughly like $\ln(\omega_i)$ for lower frequencies. The frequency at which this change in behavior occurs is base-state dependent, with the logarithmic behavior extending closer to $\omega = 1$ in more energetic base states. The lowest value we considered was $\omega_i = 1/64$, which is still well to the right of the low-frequency energy peak. Values of χ_i for $\omega_i = 1/64$ are around 0.3, indicating that the bulk of the energy extracted is taken from the tail of the low-frequency peak, rather than from the frequencies where most of the low-frequency energy resides. The size of the advective sink is roughly halved when $\omega_i = 1/8$, but the omitted frequency band contains only <10% of the non-near-inertial KE in the system.

Perhaps an overly restrictive definition of direct extraction is that energy is extracted from the dominant frequency band of the balanced flow and transferred directly to high frequencies. A similarly restrictive definition of stimulated

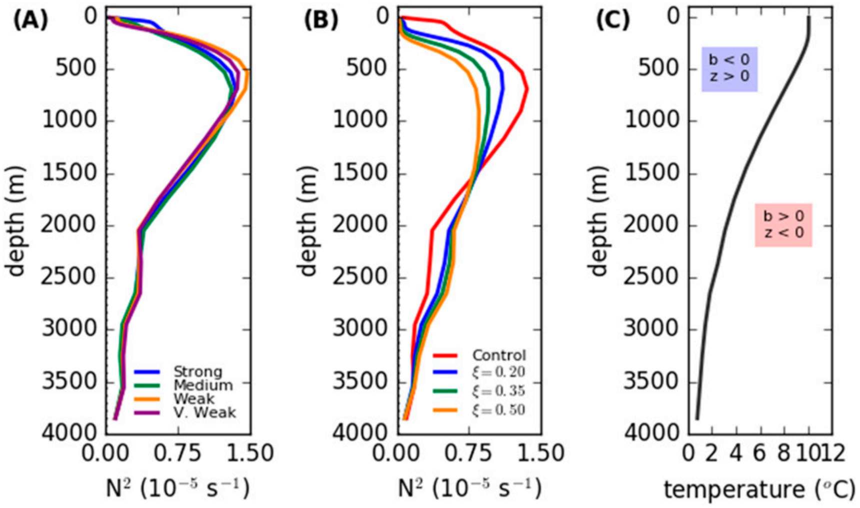

FIG. 5. A characterization of the density structure of the domain: (a) N^2 profiles for the four control runs and (b) N^2 for all values of ξ with $\tau_0 = 0.30$. (c) The reference temperature profile for the medium base state, with a schematic of $\{b, z\}$ for two parcels of water.

imbalance would have that energy cascades from low to high frequencies, passing through intermediate bands along the way. Our results suggest instead that energy is extracted out of a range of frequencies to the right of the energy-containing band and to the left of the the near-inertial band. How close to the near-inertial band this range extends is related to the strength of the base-state flow.

Figures 4c and 4d show the vertical and horizontal structure of χ_i, respectively. As the low-frequency cutoff is pushed to smaller values (paler shades of green), the amplitude of the profile shrinks, but the overall shape is fairly consistent. The horizontal structure shows a more fundamental shift: as ω_i becomes smaller, the characteristic κ of the advective sink also becomes smaller. Additionally, the amplitude of the peak shrinks, the peak itself narrows, and higher wavenumbers contribute less to the overall sink.

On the other end of the spectrum, we isolated the band around the $2f_0$ harmonic to see how it contributes to the advective sink. Wagner and Young (2016) found that a three-component model including the $2f_0$ harmonic considerably improves the results of the flow, with only a modest increase in complexity. Our model resolves many frequencies, and so naturally includes the interactions that they are explicitly including in an otherwise simplified model. Calculating the advective sink with the $2f_0$ peak omitted from the near-inertial flow results in values of χ_i that are only ~1% smaller than χ. In other words, although frequencies near $2f_0$ no doubt influence the high-frequency motion, they do not appear to be directly implicated in the advective sink.

5. Potential energy considerations

Most previous work on balanced-to-unbalanced energy transfers either has focused on kinetic energy or has made assumptions that the fluid is either barotropic (e.g., Rocha et al. 2018) or linearly stratified (e.g., Grisouard 2018). We have seen that near-inertial forcing affects the vertical energy distribution, but it also affects the vertical density profile and therefore, potential energy. Upon application of high-frequency wind forcing, the density profile begins to evolve, and this makes examining potential energy transfers more difficult. Additionally, in settings such as ours where there is a surface mixed layer, formulations of PE that are inversely proportional to N^2 become problematic.

Formally, of course, potential energy is proportional to the domain integral of density multiplied by height, and available potential energy is found by subtracting off a similar integral, but for a reference density profile. To write available potential density as a quadratic, we need to specify this reference profile, and there is some ambiguity as to how best to do so. Figure 5 shows N^2 profiles for all four control runs (Fig. 5a) and for all four strong base-state runs (Fig. 5b). These profiles are representative of the full $\{\tau_0, \xi\}$ parameter space, and clearly show that adding near-inertial forcing to the system can substantially change the N^2 profile. Specifically, the near-inertial winds flatten the N^2 profiles: local values of N^2 are significantly reduced in the upper ocean and increased in the lower ocean, especially for more energetic base states. This destratification is an ongoing but relatively stable process; the profiles are averages over the span of the time series and are representative of typical instantaneous profiles.

With these caveats in mind, we can nonetheless attempt to quantify balanced-to-unbalanced transfer of potential energy in a similar way to our calculation of χ. Except for diapycnal mixing, the buoyancy of each parcel is conserved. We thus construct a reference buoyancy profile by putting the parcel at each grid point into a temperature (or buoyancy) bin. Treating the domain like a bowl with a ridge at the bottom, we fill it from the bottom up with water from progressively warmer temperature bins. For this to be precise we evenly divide the domain into 10 000 thin horizontal slices, with careful attention paid to

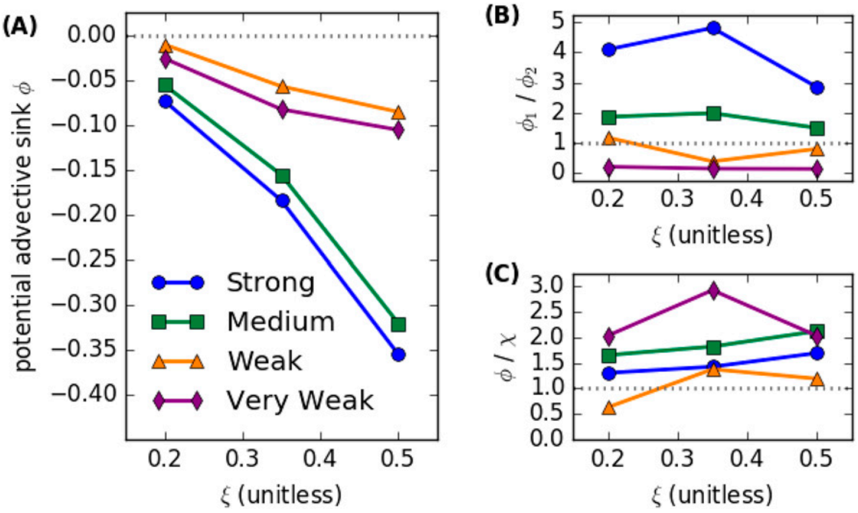

FIG. 6. The (available) potential energy sink. (a) The total sink ϕ normalized by the steady wind input into the kinetic energy, i.e., the same normalization as used in Fig. 2. Also shown are the ratio of (b) ϕ_1:ϕ_2 and (c) ϕ:χ.

the effect of the bottom topography and partial bottom cells. Each of these thin layers then has a single temperature than increases monotonically toward the surface. To get the final reference buoyancy profile, we integrate this temperature profile over each (model) vertical grid cell, again accounting for the changes in volume due to the bottom topography and the use of partial bottom cells. This results in a single buoyancy profile, $b_{\mathrm{ref}}(z)$, representing the lowest possible energy state of the fluid which is used as the reference profile for all subsequent calculations.

With this reference profile, we consider the available potential energy APE $= -bz_d$, where b is buoyancy (relative to b_{ref}) and z_d is vertical displacement of the parcel relative to its rest position; a schematic of this is shown in Fig. 5c. Since the vertical grid is relatively coarse, a spline fit is used to interpolate values of b_{ref} to calculate z more accurately than rounding to the nearest vertical grid point.[1] Note that b and z_d are opposite signed; that is, a parcel with $b > 0$ is considered to have been displaced downward. As such, APE is positive.

Given an N^2 profile that can be considered constant in time, one often derives the potential energy equation by multiplying the buoyancy equation by b/N^2. If N^2 can be considered to be slowly varying in z then one can interpret b/N^2 as an approximation for z_d. In our simulations, N^2 not only varies rapidly in z but also goes to near-zero values in the surface mixed layer. To form a potential energy equation, then, we proceed by multiplying the buoyancy equation by z_d:

$$z_d \frac{Db}{Dt} = \frac{D\mathrm{APE}}{Dt} - b\frac{Dz_d}{Dt}, \quad \text{and so} \tag{9}$$

$$\frac{D\mathrm{APE}}{Dt} = z_d \frac{Db}{Dt} + b\frac{Dz_d}{Dt}. \tag{10}$$

Unlike the kinetic energy budget, here there are two potential energy terms to consider, and there are no a priori restrictions on their relative sizes. As with the kinetic energy, the Lagrangian derivative can be expanded out using band-passed quantities, and the terms that convert balanced APE into unbalanced APE are then the potential energy analog to χ; we denote these quantities ϕ:

$$\begin{aligned} \phi &= \phi_1 + \phi_2, \quad \text{where} \\ \phi_1 &= z_d^{<}\nabla\cdot(\mathbf{v}^{>}b^{>}) \quad \text{and} \\ \phi_2 &= b^{<}\nabla\cdot(\mathbf{v}^{>}z_d^{>}). \end{aligned} \tag{11}$$

Figure 6a plots $\phi = \phi_1 + \phi_2$ as a function of ξ, using the same normalization as Fig. 2 (i.e., the total wind power input of the matching control simulation). As with χ, ϕ acts as a sink of balanced potential energy for all base states and all values of ξ, with larger sinks associated with more energetic base states. Figure 6b shows the ratio of ϕ_1 to ϕ_2. The robustly positive values indicate that ϕ_1 and ϕ_2 have the same sign, and as such both terms extract balanced potential energy. For energetic base states ϕ_1 is dominant but for weaker base states, the two terms are comparable in size. If the potential energy equation is formed by multiplying the buoyancy equation by a factor of b/N^2 (rather than z_d), only ϕ_1 is available to extract balanced potential energy. In energetic systems where $\phi_1 \gg \phi_2$, using $\phi \sim \phi_1$ may be a sufficient approximation, but in relatively quiescent systems it will not be robust.

Figure 6c plots the ratio of ϕ to χ. This ratio is $O(1)$, with PE extraction typically being somewhat larger than KE extraction. If we think of the balanced flow as quasigeostrophic plus a

---

[1] The fine vertical grid used to calculate the reference profile in the first place is not used directly, since what is actually integrated in the model is the 30-point vertical grid and not the 10 000-slice reworking. If the method for generating the reference profile is altered, the method to calculate z with respect to that reference profile remains the same.

higher-order correction, then a loss of balanced energy implies a loss of quasigeostrophic energy. The PE-to-KE ratio of energy in a given vertical mode is then well approximated by $(L/L_d)^2$, where L is the horizontal length scale from which kinetic energy is extracted and L_d is the deformation radius for the vertical mode in question; L_d for the first baroclinic mode is ~20 km for all four base states. If energy were being extracted primarily from the first baroclinic mode, for example, then transfer spectra for χ and ϕ should show a peak values at wavelengths slightly larger than $2\pi \times 20$ km. Corrections to quasigeostrophy can, of course, alter KE-to-PE ratios. Moreover, the analysis becomes more complex in that balanced energy is also extracted from barotropic and higher baroclinic modes. We were not able to unambiguously assess the characteristic length scale of the potential energy transfer due to difficulties in calculating transfer spectra below the level of the topography. Nonetheless, integrating above the topography, we find that most balanced potential energy is lost at $\sim\kappa = 9$, with an additional broad sink that spans wavenumbers up to $\kappa \sim 50$ (not shown). This is broadly consistent with the idea that energy is being extracted from the first few vertical modes at length scales slightly larger than the relevant deformation scale. Although this picture must be taken as qualitative at best, it suggests interesting questions to pursue with a system better designed to look at the potential energy transfer.

6. Discussion

Consistent with the eddy-permitting results of TS16, we find that forcing an eddy-resolving primitive equation model in the near-inertial band induces Reynolds stresses that transfer energy from the balanced kinetic energy to the near-inertial KE. This advective sink removed balanced kinetic energy from a range of horizontal wavenumbers close to $\kappa \sim 30$ for all base states, which corresponds to energy being removed from length scales near the deformation radius. The magnitude of this energy transfer depends both on the amount of near-inertial forcing and on the strength of the base state, with more energetic base states and stronger near-inertial forcing resulting in larger sinks. For energetic base states and strong near-inertial winds, the advective sink can extract nearly a third of the power input by the steady winds, with number dropping to about 5% in our weakly forced simulations. This sink of kinetic energy was offset, however, by a low-frequency buoyancy production of kinetic energy, i.e., by transfer from low-frequency potential to kinetic energy. The net result was a slight increase in low-frequency kinetic energy following addition of near-inertial winds.

Barkan et al. (2017) introduced the terms "direct extraction" and "stimulated imbalance." The former corresponds to energy being transferred directly from low to high frequencies, whereas the latter involves balanced energy being first transferred to intermediate frequencies. They considered a strongly forced regime and used Gaussian filtering to separate the flow into high-, intermediate-, and low-frequency bands to find that about half of the balanced-to-unbalanced energy transfer they observed came from direct extraction and half from stimulated imbalance. We did a similar analysis, but used Fourier techniques and several frequency bands to get a more detailed picture of which frequencies of balanced flow are losing energy. We found that, for a range frequencies used to define the high-frequency end of the low-frequency band, χ_i varied like $\ln(\omega_i)$. The cutoff of this intermediate frequecy band varied from $\omega_i = 1/64$ ($\sim f/128$, the lowest value we tested) up to $\omega_i = 1/2$ ($\sim f/4$), with the high-frequency end of this band increasing for stronger base states. In other words, over this range of frequencies each frequency band contributes equally to the advective sink. Perhaps unsurprisingly, lower-frequency bands were associated with larger horizontal scales.

TABLE A1. Domain-integrated sources and sinks of the kinetic energy budget for the full flow with $\tau_0 = 0.15$.

Term	Control	$\xi = 0.2$	$\xi = 0.35$	$\xi = 0.5$
Steady wind	1.00	0.97	0.95	0.94
HF wind	0.00	0.36	0.98	1.80
Bottom drag	−0.66	−0.82	−0.88	−1.02
Buoyancy production	−0.056	0.065	0.068	0.086
Horizontal viscosity	−0.0001	−0.0002	−0.0002	−0.0003
Vertical viscosity	−0.28	−0.55	−1.02	−1.67
Residual	0.004	0.025	0.10	0.13

How to interpret our results in the context of theoretical models such as those of XV15 and Wagner and Young (2016) is not entirely clear. These models make use of velocities based on Lagrangian averaging that are difficult for us to access in model simulations. Also numerically difficult is that potential energy in these models is inversely proportional to N^2, which can be near zero in the mixed layer. These models conserve wave action or, effectively, wave kinetic energy. If we take this to imply that there should be no net transfer into or out of the $\mathrm{KE}^{>}$ pool using our Eulerian statistics, then this conservation seems to suggest that χ_{HF} should be balanced by a buoyancy transfer from $\mathrm{KE}^{>}$ to $\mathrm{PE}^{>}$. In some simulations, we did find such an approximate balance (to within about 25%) between these two terms; however, the result was not at all robust. In other simulations, for example, these two transfers were of the same sign (i.e., both were source terms of $\mathrm{KE}^{>}$, not shown).

Although our system is not well suited for a detailed study of potential energy, we nonetheless attempted to quantify ϕ, a potential energy analog to the advective sink, χ. We found the ratio ϕ/χ to be $O(1)$, with potential energy transfers typically being the larger of the two. If we think of balanced energy as being extracted from the first few baroclinic modes, then this ratio is consistent with extraction from scales slightly larger than the relevant deformation radii. Although we were unable to verify this speculation in detail, it was the case that energy was extracted from balanced flow at horizontal scales somewhat larger than the deformation radius.

It is clear, from a range of work done using different models an in a variety of regimes, that near-inertial motion can induce balanced-to-unbalanced transfers of both kinetic and potential energy. These transfers, however, tend to be to be small (e.g., Asselin and Young 2020). Indeed, in our simulations, the bulk of dissipation for the balanced flow comes from bottom drag. Our simulations also suggest that near-inertial motion can also redistribute balanced energy vertically. Additionally, and

TABLE A2. As in Table A1, but for the balanced flow. Geostrophic flow is used to calculate the wind, drag, and viscous terms, and the low-frequency flow is used to calculate the buoyancy production and advective sink terms. Wind input from high-frequency winds is small and so is not listed.

Term	Control	$\xi = 0.2$	$\xi = 0.35$	$\xi = 0.5$
Steady wind	0.72	0.70	0.70	0.70
Bottom drag	−0.62	−0.69	−0.65	−0.68
Buoyancy production	−0.05	0.09	0.15	0.27
Advective sink	0.00	−0.03	−0.09	−0.15
Vertical viscosity	−0.02	−0.03	−0.05	−0.08
Horizontal viscosity	−0.000 01	−0.0002	−0.0002	−0.0003
Residual	0.03	0.04	0.06	0.06

perhaps more importantly, near-inertial forcing also has a profound effect on the stratification. With this in mind, it would be interesting to consider how phase-averaged models might be extended to allow for time-varying stratification and surface mixed layer effects. Finally, looking for these interactions in observations may be fruitful, for example, by extending studies such as Rocha et al. (2016) and Wang et al. (2019) to specifically consider the impact of near-inertial motion on balanced flow.

Acknowledgments. This work was supported by NSERC Discovery Grant 222363. Computational resources were provided by CLUMEQ and Compute Canada. We also thank two anonymous reviewers, whose thoughtful critiques and suggestions greatly improved this paper, and O. Asselin and G. Wagner for their helpful conversations.

APPENDIX

Details of Full and Low-Frequency Kinetic Energy Budgets

Figure 2 shows the (normalized) trends for the steady wind stress input, bottom drag, advective sink, and buoyancy production in the balanced kinetic energy budget. However, neither of the viscous terms are included because they are small, and the full budget is not shown. For reference, Tables A1 and A2 list the full and balanced budgets (including the two viscous terms) for the medium base state.

REFERENCES

Alford, M., 2001: Internal swell generation: The spatial distribution of energy flux from the wind to the mixed layer near-inertial motions. *J. Phys. Oceanogr.*, **31**, 2359–2368, https://doi.org/10.1175/1520-0485(2001)031<2359:ISGTSD>2.0.CO;2.

——, 2003: Redistribution of energy available for ocean mixing by long-range propagation of internal waves. *Nature*, **423**, 159–162, https://doi.org/10.1038/nature01628.

——, J. A. MacKinnon, H. L. Simmons, and J. D. Nash, 2016: Near-inertial internal gravity waves in the ocean. *Annu. Rev. Mar. Sci.*, **8**, 95–123, https://doi.org/10.1146/annurev-marine-010814-015746.

Asselin, O., and W. R. Young, 2019: An improved model of near-inertial wave dynamics. *J. Fluid Mech.*, **876**, 428–448, https://doi.org/10.1017/jfm.2019.557.

——, and ——, 2020: Penetration of wind-generated near-inertial waves into a turbulent ocean. *J. Phys. Oceanogr.*, **50**, 1699–1716, https://doi.org/10.1175/JPO-D-19-0319.1.

Barkan, R., K. B. Winters, and J. C. McWilliams, 2017: Stimulated imbalance and the enhancement of eddy kinetic energy dissipation by internal waves. *J. Phys. Oceanogr.*, **47**, 181–198, https://doi.org/10.1175/JPO-D-16-0117.1.

Bühler, O., and M. E. McIntyre, 2005: Wave capture and wave–vortex duality. *J. Fluid Mech.*, **534**, 67–95, https://doi.org/10.1017/S0022112005004374.

Furuichi, N., T. Hibiya, and Y. Niwa, 2008: Model-predicted distribution of wind-induced internal wave energy in the world's oceans. *J. Geophys. Res.*, **113**, C09034, https://doi.org/10.1029/2008jc004768.

Gertz, A., and D. N. Straub, 2009: Near-inertial oscillations and the damping of mid-latitude gyres: A modeling study. *J. Phys. Oceanogr.*, **39**, 2338–2350, https://doi.org/10.1175/2009JPO4058.1.

Grisouard, N., 2018: Extraction of potential energy from geostrophic fronts by inertial-symmetric instabilities. *J. Phys. Oceanogr.*, **48**, 1033–1051, https://doi.org/10.1175/JPO-D-17-0160.1.

——, and L. N. Thomas, 2015: Critical and near-critical reflections of near-inertial waves off the sea surface at ocean fronts. *J. Fluid Mech.*, **765**, 273–302, https://doi.org/10.1017/jfm.2014.725.

——, and ——, 2016: Energy exchanges between density fronts and near-inertial waves reflecting off the ocean surface. *J. Phys. Oceanogr.*, **46**, 501–516, https://doi.org/10.1175/JPO-D-15-0072.1.

Huang, R. X., W. Wang, and L. L. Liu, 2006: Decadal variability of wind-energy input to the world ocean. *Deep-Sea Res. II*, **53**, 31–41, https://doi.org/10.1016/j.dsr2.2005.11.001.

Jiang, J., Y. Lu, and W. Perrie, 2005: Estimating the energy flux from the wind to ocean inertial motions: The sensitivity to surface wind fields. *Geophys. Res. Lett.*, **32**, L15610, https://doi.org/10.1029/2005GL023289.

Josey, S. A., E. C. Kent, and P. K. Taylor, 2002: Wind stress forcing of the ocean in the soc climatology: Comparisons with the NCEP-NCAR, ECMWF, UWM/COADS, and hellerman and rosenstein datasets. *J. Phys. Oceanogr.*, **32**, 1993–2019, https://doi.org/10.1175/1520-0485(2002)032<1993:WSFOTO>2.0.CO;2.

Kafiabad, H. A., and P. Bartello, 2018: Spontaneous imbalance in the non-hydrostatic boussinesq equations. *J. Fluid Mech.*, **847**, 614–643, https://doi.org/10.1017/jfm.2018.338.

Large, W., J. McWilliams, and S. Doney, 1994: Oceanic vertical mixing: A review and a model with a nonlocal boundary layer parameterization. *Rev. Geophys.*, **32**, 363–403, https://doi.org/10.1029/94RG01872.

Li, M., J. Liu, Z. Wang, H. Wang, Z. Zhang, L. Zhang, and Q. Yang, 2013: Assessment of sea surface wind from NWP reanalyses and satellites in the southern ocean. *J. Atmos. Oceanic Technol.*, **30**, 1842–1853, https://doi.org/10.1175/JTECH-D-12-00240.1.

Rimac, A., J.-S. von Storch, C. Eden, and H. Haak, 2013: The influence of high-resolution wind stress fields on the power input to near-inertial motions in the ocean. *Geophys. Res. Lett.*, **40**, 4882–4886, https://doi.org/10.1002/grl.50929.

Rocha, C. B., T. K. Chereskin, S. T. Gille, and D. Menemenlis, 2016: Mesoscale to submesoscale wavenumber spectra in drake passage. *J. Phys. Oceanogr.*, **46**, 601–620, https://doi.org/10.1175/JPO-D-15-0087.1.

——, G. L. Wagner, and W. R. Young, 2018: Stimulated generation: Extraction of energy from balanced flow by near-inertial waves. *J. Fluid Mech.*, **847**, 417–451, https://doi.org/10.1017/jfm.2018.308.

Scott, R. B., and Y. Xu, 2009: An update on the wind power input to the surface geostrophic flow of the world ocean. *Deep-Sea Res. I*, **56**, 295–304, https://doi.org/10.1016/j.dsr.2008.09.010.

Taylor, S., and D. Straub, 2016: Forced near-inertial motion and dissipation of low-frequency kinetic energy in a wind-driven channel flow. *J. Phys. Oceanogr.*, **46**, 79–93, https://doi.org/10.1175/JPO-D-15-0060.1.

Thomas, L. N., 2012: On the effects of frontogenetic strain on symmetric instability and inertia-gravity waves. *J. Fluid Mech.*, **711**, 620–640, https://doi.org/10.1017/jfm.2012.416.

Tulloch, R., J. Marshall, and K. S. Smith, 2009: Interpretation of the propagation of surface altimetric observations in terms of planetary waves and geostrophic turbulence. *J. Geophys. Res.*, **114**, C02005, https://doi.org/10.1029/2008JC005055.

Wagner, G., and W. Young, 2016: A three-component model for the coupled evolution of near-inertial waves, quasi-geostrophic flow and the near-inertial second harmonic. *J. Fluid Mech.*, **802**, 806–837, https://doi.org/10.1017/jfm.2016.487.

Wang, P., Z. He, K. R. Thompson, and J. Sheng, 2019: Modulation of near-inertial oscillations by low-frequency current variations on the inner scotian shelf. *J. Phys. Oceanogr.*, **49**, 329–352, https://doi.org/10.1175/JPO-D-18-0047.1.

Whitt, D. B., and L. N. Thomas, 2013: Near-inertial waves in strongly baroclinic currents. *J. Phys. Oceanogr.*, **43**, 706–725, https://doi.org/10.1175/JPO-D-12-0132.1.

——, and ——, 2015: Resonant generation and energetics of wind-forced near-inertial motions in a geostrophic flow. *J. Phys. Oceanogr.*, **45**, 181–208, https://doi.org/10.1175/JPO-D-14-0168.1.

Xie, J.-H., and J. Vanneste, 2015: A generalised-Lagrangian-mean model of the interactions between near-inertial waves and mean flow. *J. Fluid Mech.*, **774**, 143–169, https://doi.org/10.1017/jfm.2015.251.

Young, W., and M. Ben Jelloul, 1997: Propagation of near-inertial oscillations through a geostrophic flow. *J. Mar. Res.*, **55**, 735–766, https://doi.org/10.1357/0022240973224283.

Zhai, X., H. L. Johnson, D. P. Marshall, and C. Wunsch, 2012: On the wind power input to the ocean general circulation. *J. Phys. Oceanogr.*, **42**, 1357–1365, https://doi.org/10.1175/JPO-D-12-09.1.